Journal of Applied Fluid Mechanics, Vol. 13, No. 2, pp. 667-678, 2020.
Available online at www.jafmonline.net, ISSN 1735-3572, EISSN 1735-3645.
DOI: 10.29252/jafm.13.02.30408

On the Application of Endoscopic Background-Oriented Schlieren Technique for Near-Field Investigation of Density Field

M. Zare, S. M. Mousavi, A. Mohseni† and A. H. Nikjoo

Faculty of Mechanical and Energy Engineering, Shahid Beheshti University (SBU), Bahar Blvd., Hakimieh, Tehran, Postal Code 16589-53571, Iran

†*Corresponding Author Email: ar_mohseni@sbu.ac.ir*

(Received April 18, 2019; accepted July 18, 2019)

ABSTRACT

Background-Oriented Schlieren (BOS) is a non-intrusive and non-destructive technique for measuring density gradient in transparent media. Given the dependency of the refractive index and density of a medium, its static density field can be determined as a secondary measurand from BOS measurements. For an ideal gas, if the pressure variation is negligible, the static temperature field can be determined as a tertiary measurand. While the BOS technique for far-field measurements has been extensively researched, the implementation of this technique for near-field measurements still needs to be investigated. Near-field BOS is especially important for the measurement and visualization of internal flows, such as turbomachine flows, in which access to flow passage is limited and might be feasible using endoscopes (borescopes). This paper presents the features and challenges of the endoscopic BOS technique and presents methods and solutions for the application of this method in near-field measurements. The features of endoscopic BOS records as well as the comparison of endoscopic BOS and BOS measurements with camera are presented.

Keywords: Endoscopic background-oriented schlieren; Density measurement; Endoscope; Borescope; Near-field measurement.

NOMENCLATURE

BOS	Background-Oriented Schlieren
$\mathscr{C}_d$	discrete correlation function
d	nominal dot pattern diameter
f	focal length
GRIN	gradient index lens
$K(\lambda)$	Gladstone-Dale constant
I	light intensity
I_0	light intensity at the center of a Gaussian pattern
M	magnification factor
n	refractive index
n_0	refractive index of surrounding environment
PIV	Particle Image Velocimetry
$\vec{r}$	position vector in the image plane at $z = z_b + z_i, \vec{r} = (x, y)$
$S(x, y)$	source term of Poisson's Eq. (4)
S/N	signal-to-noise ratio
V3V	Volumetric 3-Component Velocimetry
x, y, z	coordinate components of the right-handed Cartesian coordinate system O_{xyz} in Fig. 1
$\mathbb{Z}$	the set of integer numbers
z_1	begin of test medium along the z-axis
z_2	end of test medium along the z-axis
z_b	position of lens along the z-axis
z_d	middle of test medium along the z-axis
z_i	distance of image plane from lens along the z-axis
δ	magnitude of displacement or shift vector $\vec{\delta}$
$\vec{\delta}$	displacement or shift vector in image plane
δ_x, δ_y	components of the shift vector $\vec{\delta}$ in image plane
Δy_i	displacement in y direction in image plane, $\Delta y_i \equiv \delta_y$
ε	deflection angle between a light beam and the z-axis
ε_x	deflection angle of a light beam in xz-plane

ε_y	deflection angle of a light beam in yz-plane	λ	wavelength of light
ρ	(static) fluid density		

1. INTRODUCTION

With advancements in different branches of fluid dynamics specially aerodynamics, the development of advanced measurement techniques for investigating fluid flow phenomena in laboratory-scale as well as full-scale has gained increasing attention during past two decades. In this regard, researchers have been trying to make use of new technologies to develop and improve new measurement techniques to quantify fluid phenomena. Due to their accuracy, resolution, and non-intrusiveness, optical and image-based measurement techniques have received special attention and several measurement techniques such as Particle Image Velocimetry (PIV), Volumetric 3-Component Velocimetry (V3V), and Background-Oriented Schlieren (BOS) measurement technique have emerged from research works.

Optical measurement techniques benefit from the advantage of providing detailed information of flow fields without intrusion. Although their implementation can be very demanding, several optical techniques such as schlieren method, Moirè technique, interferometry, optical tomography etc. have been developed during the past decades. These methods are based on changes in refractive index and are able to provide quantitative data of density variation in transparent media, Tropea *et al.* (2007), Settles (2001). Early measurement systems based on these methods, needed high quality mirrors and lenses with sizes comparable to the volume under investigation. Although these traditional methods are still in use, Saiprakash *et al.* (2019), Heidari *et al.* (2010), due to the delicacy and sensitivity of their optical setup and measurement costs, their applications are limited to small and often laboratory scale measurements and wind tunnel investigations. These methods are often not suitable for industrial or large-scale applications and are more suited for flow visualization and qualitative rather than quantitative investigations, Ota *et al.* (2015).

These limitations have placed the need for the development of simpler methods, such as Background-Oriented Schlieren (BOS) technique. In 1999, Meier (1999) introduced the BOS technique, which can capture the density variation of a transparent flow field with a simple setup, which is less sensitive to settings and ambient conditions than the traditional methods. BOS can be described as a simpler form of schlieren technique. This technique has been used in a wide range of applications such as wind tunnel, Meier (2002), Venkatakrishnan and Meier (2004), supersonic flow, Venkatakrishnan and Meier (2004), free jet flow, Goldhahn and Seume (2007), Tipnis *et al.* (2013), helicopter blade tip vortex measurement in full-scale, Kindler *et al.* (2007), Bauknecht *et al.* (2014), and heat transfer investigations, Skornyakova *et al.* (2004).

Unlike traditional optical measurement methods, BOS incorporates numerical computation for the analysis of measured data. The required computational time has been considerably reduced because of rapid progress in computation power and fast correlation algorithms, Meier (2002). The BOS technique has the potential to eliminate the restrictions on the size of test section and has been implemented for real-scale outdoor measurements, Hargather and Settles (2010), Richard *et al.* (2002). In outdoor large-scale applications, natural scenes could be used as background instead of artificial background in this measurement technique. Hargather and Settles (2010) studied the application and characteristics of natural backgrounds such as corn field and trees.

Owed to the available imaging technology, BOS can be used for qualitative and quantitative analyses of unsteady density fields in compressible flows at high Mach numbers. Richard *et al.* (2002) studied the use of this method to obtain fluid density in a supersonic flow and also the structure of turbulent flames with a maximum temperature of 1500°c. Vinnichenko *et al.* (2014) studied the application of BOS to investigate the heat transfer at the contact surface of fluid and gas. Similarly, Tipnis *et al.* (2013) used this method to obtain the density field in a supersonic rectangular jet. The application of BOS to measure explosion shock waves has been reported by Sommersel *et al.* (2008). Su and Bai (2016) have used BOS to measure the internal fire whirl for high-rise building design. Another application of BOS is the investigation of tip vortices of blades, which can play an important role in the optimization of turbomachinery. Kindler *et al.* (2007) used this method to measure the tip vortices of rotor blades of a helicopter.

Using tomography techniques, the BOS data obtained from different orientations of the same transparent medium can be integrated into a volumetric density gradient field. Berger *et al.* (2009) used this method to model the gas flow around moving objects and Ota *et al.* (2011) investigated a supersonic flow around a symmetrical body.

The implementation of optical measurement techniques for measurement in internal flows such as turbomachinery flows is faced with several technical challenges including provision of optical access, background illumination, high pressure and high temperature flow conditions, casing vibration (e.g. in turbomachines), image distortion, small test sections etc. This paper presents the feasibility of the endoscopic BOS measurement technique and investigates the challenges of near-field measurements. Flow passages can be accessed directly by camera through a window or indirectly

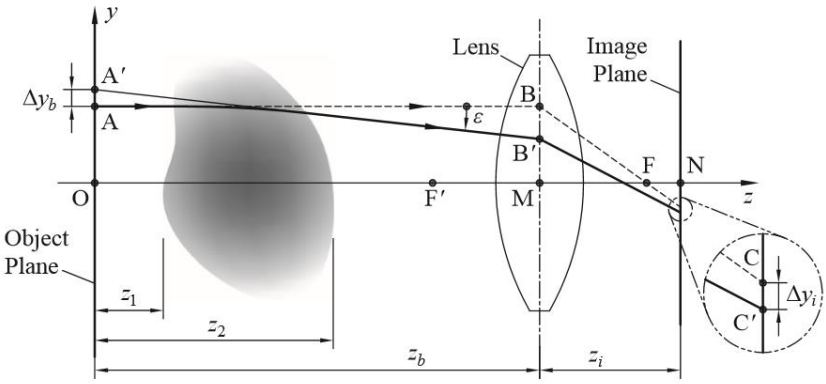

Fig. 1. Schematic of a typical BOS measurement setup.

via an endoscope. Endoscopes (a.k.a. borescopes) facilitate accessing a flow channel greatly. However, due to small aperture and the quality and design of optical path, recorded images by endoscopes may suffer from decreased signal-to-noise (S/N) ratio and image distortion, as compared with images recorded directly by camera. In the following, the characteristics of endoscopic BOS are investigated.

2. BACKGROUND-ORIENTED SCHLIEREN MEASUREMENT TECHNIQUE

The background-oriented schlieren (BOS) technique uses the deflection of light rays passing thorough a transparent test medium with varying refractive index. Since the change in refractive index is dependent on density gradient, measured light ray deflections can be used to determine the density gradient and, subsequently, the density of a medium. Compared to other density measurement techniques, BOS has a relatively simple and versatile setup, which increases the feasibility of its application in various measurements, Richard *et al.* (2002), Goldhahn *et al.* (2009).

A common BOS setup consists of a digital camera, a calibration plane, a background plane with a random dot pattern, and one or multiple light sources. A typical measurement configuration is illustrated in Fig. 1. A camera (consisting of a lens and an image sensor at the image plane) captures the random dot pattern, placed at the object plane, in the absence and in the presence of a test medium, depicted as a gray gradient in the test section between z_1 and z_2. In the absence of the test medium, the optical configuration is at its reference state and a light ray from point A in Fig. 1, which passes through a base or surrounding medium (usually air) with homogeneous refractive index on the ABC path, is registered at point C on the image plane. With the presence of a transparent test medium, the path of the light ray may change due to the variation of the refractive index of the medium. For a continuous gradual variation of refractive index, the path of the light ray is distorted to AB′C′, causing a shift in the image of point A from C to C′ on the image sensor in the image plane. In the absence of the test medium, C′ is the image of A′ in the object plane. If the relation of the refractive index and the density of medium is known, the analysis of these shifts can result in the density variation of the medium.

In practice, first a pattern of random dots is generated and is used as background image. Then, the camera takes a picture from the background in the absence of the test medium. This image is the reference image of the measurement. Then, an image of the background is taken in the presence of the test medium. Ideally the shifts in the dot patterns between these images contains the information of the variation of refractive index in the test medium, Raffel *et al.* (2007).

In gasses, the dependency between gas density, ρ, and its refractive index, n, is provided by the Gladstone-Dale equation, Merzkirch (1987), Venkatakrishnan and Meier (2004):

$$n\text{-}1 = K(\lambda)\,\rho \tag{1}$$

where $K(\lambda)$ is the Gladstone-Dale constant and λ is the wavelength of light.

As shown in Fig. 1, points C and C′ represent the images of point A in the absence and presence of the test medium, respectively. If the beam deflection angle, ε_y, is small so that the paraxial approximation is valid, Saleh and Teich (2007), the relation between beam deflection angle and displacement of the image of a typical point C in the image plane, Δy_i, is:

$$\Delta y_i = z_d M\,\varepsilon_y \tag{2}$$

where $z_d = (z_1 + z_2)/2$ is the approximate distance of the test medium from the background image or the object plane, and $M = z_i/z_b$ is the magnification factor, Richard and Raffel (2001), Richard *et al.* (2002), Raffel (2015). If the width of the medium is considerably smaller than the distance of the object plane to camera lens, i.e. $\Delta z = z_2 - z_1 \ll z_b$, and if the distance of medium to the lens, $z_b - z_d$, is long enough so that the image is located approximately at the focal point of the lens, $z_i \approx \overline{\mathrm{MF}} = f$, where f is the focal length of the lens, then, Venkatakrishnan and Meier (2004):

$$\varepsilon_y \approx \frac{z_b \Delta y_i}{z_d f} \approx \frac{1}{n_0}\int_{z_1}^{z_2} \frac{\partial n}{\partial y} dz \tag{3}$$

In this equation n_0 is the refractive index of the surrounding medium (often air). A similar equation can be written to obtain the deflection angle in the *xz* plane. For a gas, it follows that these displacements in the *xy* plane determine the density gradient at each point of the plane by Poisson's equation, Venkatakrishnan and Meier (2004):

$$\frac{\partial^2}{\partial x^2}\rho(x,y) + \frac{\partial^2}{\partial y^2}\rho(x,y) = S(x,y) \tag{4}$$

where $S(x,y)$ is the source term that is calculated at each point from the displacements obtained by correlation analysis. The main steps in measuring a density field are:

1. Determination of the displacement of background patterns in the presence of a test medium with respect to their positions at reference state. These displacement vectors represent the refractive index gradient at each point.
2. Calculation of the density field by solving the Poisson's Eq. (4).

2.1 Reference Image

For determining the displacement or shift vectors by correlation analysis (sec. 2.2), the background or reference image should contain a pattern of randomly distributed discrete or partially overlapping points. The concentration of these patterns is selected such that while not overlapping or just partially overlapping, they are as close to each other as possible. In addition, the size of the dot patterns in the background plane is chosen such that the image of each dot pattern in the camera becomes at least three pixels wide in each direction. The randomization of the dot patterns in this study was achieved using the randomization function of the C++ programming language.

In order to minimize the effects of digitization and noise in digital image records and to increase the accuracy of position estimation for each point, the points were marked by Gaussian or bell-shaped light intensity distribution patterns, $I(x,y)$, Raffel *et al.* (2007):

$$I(x,y) = I_0 \exp\left(-\frac{(x-x_0)^2 + (y-y_0)^2}{d^2/8}\right) \tag{5}$$

where I_0 is the light intensity at the center of the Gaussian distribution located at the position of the point (x_0, y_0) in the Cartesian coordinates (x,y) in the image plane, and d is the nominal dot pattern diameter. In an 8-bit image, I_0 is 255 or less. A typical background image with random Gaussian dot patterns is depicted in Fig. 2.

2.2 Calculation of Displacement Vectors

In images of random distribution of distinct dot patterns, correlation algorithms are commonly used to estimate particle shifts between two images. Each image is subdivided into small windows known as interrogation windows, in which particle shifts can be approximated by a translation vector. The displacement vector field results from the correlation analysis of all interrogation window pairs of two background images one at reference state and the other in the presence of test medium. In Fig. 3, image 1 is the image of background plane in reference state, and image 2 is its image in the presence of a test medium. Cross-correlation analysis of interrogation windows, selected from the same positions in each image, can result in the translation or displacement vectors. The displacement vector field of the entire image results from estimating the displacement vectors of individual pairs of interrogation windows. The interrogation windows may partially overlap to increase the resolution of the estimated displacement vectors.

For two normalized gray-scale interrogation windows, in which light intensity varies between 0 and 1, let $I_1(\vec{r})$ and $I_2(\vec{r})$ indicate the normalized light intensity distributions at point $\vec{r} = (x,y)$ in interrogation windows 1 and 2, respectively. Discrete cross-correlation is defined as:

$$\mathscr{C}_d\,[I_1, I_2](i,j,\delta_x,\delta_y) = \frac{\sum_i \sum_j \left[I_1(i,j) I_2(i+\delta_x, j+\delta_y)\right]}{\sqrt{\sum_i \sum_j I_1^2(i,j)}\sqrt{\sum_i \sum_j I_2^2(i+\delta_x, j+\delta_y)}} \tag{6}$$

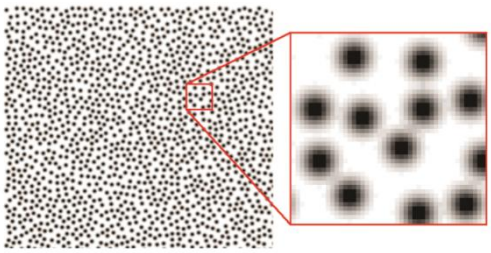

Fig. 2. A typical background image with random Gaussian dot patterns. The image color is inverted for printing.

and provides an estimate of the translation vector $\vec{\delta}$, at which $\mathscr{C}_d$ is maximized, Raffel *et al.* (2007).

In this definition $\vec{\delta} = (\delta_x, \delta_y) \in \mathbb{Z}^2$ is an integer displacement vector (with pixel accuracy) in image plane, and the sums are taken over the entire range of each index. For each assumed translation (δ_x, δ_y), the sum of all light intensity products of overlapping pixels result in a cross correlation value $\mathscr{C}_d(\delta_x, \delta_y)$. If the actual relative displacement of interrogation windows is small enough so that the images of the interrogation window pair are correlated, then the cross-correlation function, Eq. (6), is maximized, when $\vec{\delta}$ is nearest to the average particle image or dot pattern shift within the interrogation windows, Raffel *et al.* (2007). Using interpolation techniques, the displacement vector $\vec{\delta}$ can be estimated with sub-pixel accuracy.

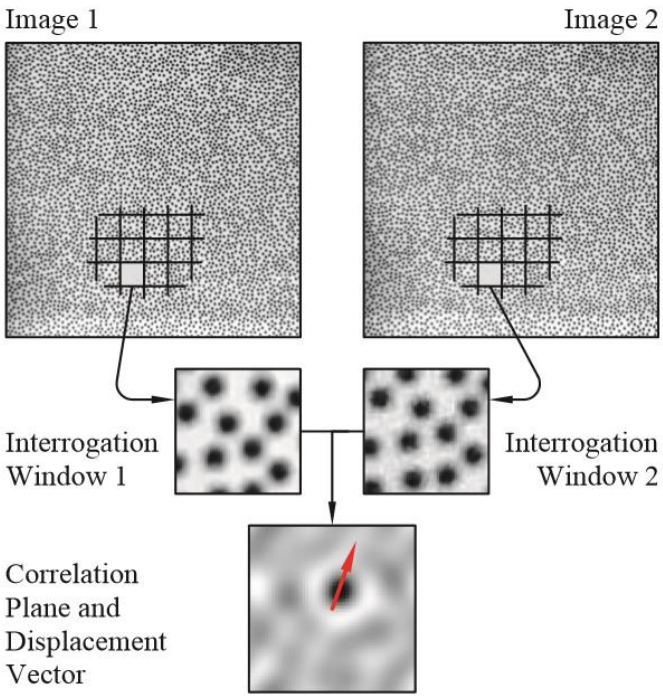

Fig. 3. Cross-correlation Analysis. The displacement vector is estimated by correlation analysis of two interrogation windows extracted from the same position in each image. The image color is inverted for printing.

Cross-correlation between two interrogation windows can only result in one displacement vector, which is the average linear shift of dots in the interrogation windows. Therefore, the size of interrogation window should be small enough that the displacement of dot patterns can be assumed linear to an acceptable approximation.

3. ENDOSCOPIC BOS MEASUREMENTS

Endoscopes (a.k.a. borescopes) are used to provide access to the interior of pipes, machines etc. which are not accessible by naked eye or regular cameras for visual inspection. In this section the implementation of borescopes for near-field BOS measurements is presented.

3.1 Types of Endoscopes

Endoscopes provide an optical link between a subject and a recording device with a cylindrical or tubular geometry. Rigid endoscopes, Fig. 4, are generally of cylindrical shape with a subject objective at one end and an eyepiece at the other end. Hopkins lens array or gradient index lens (GRIN) can be used to provide optical link between both ends of endoscope. Such endoscopes are straight, non-flexible, and cannot bend to pass through curved access ports.

Flexible borescopes, on the other hand, are designed to pass through non-straight openings. To allow flexibility and articulation, a bundle of optical glass fibers relay the acquired image to an eyepiece in flexible borescopes, Fig. 5. In both rigid and flexible borescopes, the illumination of field of view is realized by guiding light via a bundle of optical glass fibers towards the subject end of borescope. Different fields of view, Fig. 6, and directions of view, Fig. 7, are available at the subject side to provide optical access to confined regions.

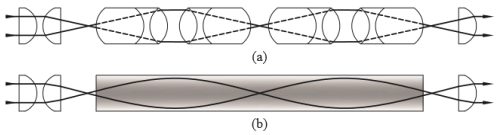

Fig. 4. Optical construction of rigid borescope. (a) With Hopkins lens array, (b) with gradient index lens (GRIN) [www.gradientlens.com].

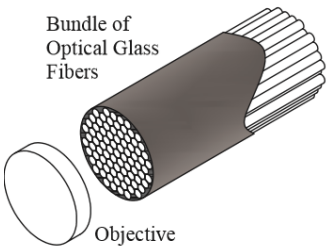

Fig. 5. Schematic construction of flexible borescope.

3.2 Endoscopic Image Records

The distinctive features of borescope records with respect to camera images are reduced illumination

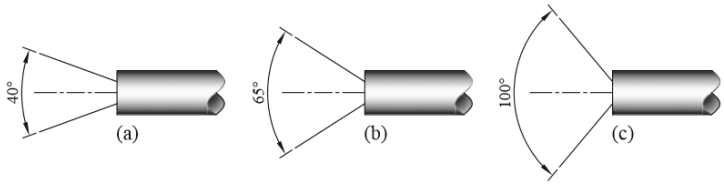

Fig. 6. Typical field of view angles of borescopes.

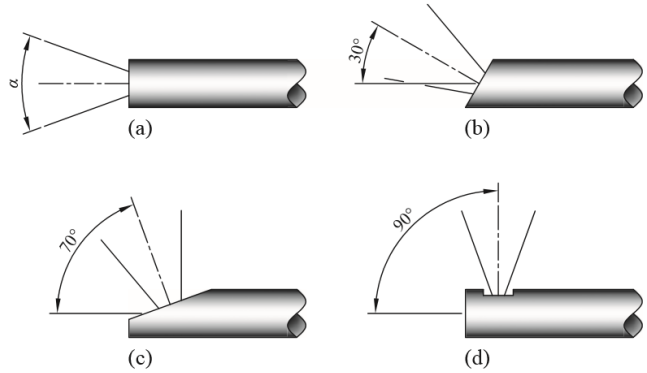

Fig. 7. Typical directions of view of borescopes.

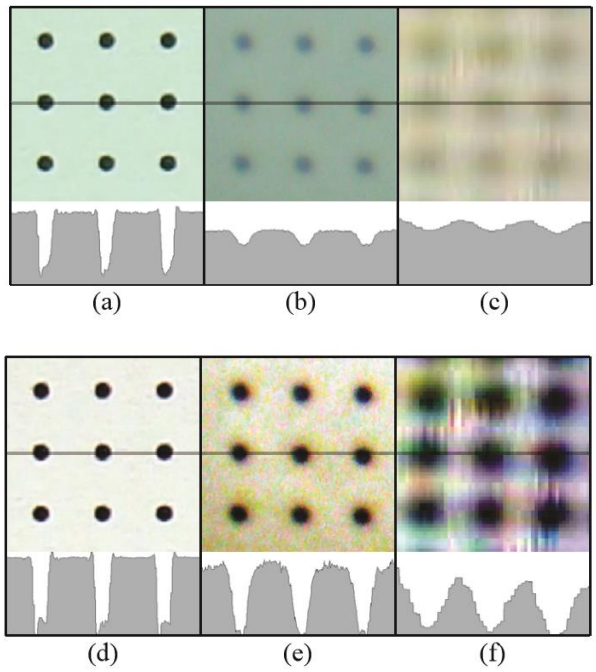

Fig. 8. Comparison of calibration images recorded by (a) camera, (b) rigid borescope, and (c) flexible borescope, and their enhancements by image processing, (d) to (f). The intensity variation diagram along the horizontal line passing through the image center is shown beneath each image.

and increased distortion of recorded images. Reduction of light intensity causes the reduction of S/N ratio and is due to the small aperture of borescope and the length and construction of optical path and optical path components. Image distortion can be due to optical design, manufacturing tolerances, and quality of optical components. In flexible borescopes, in which image is relayed by optical glass fibers, each fiber represents a pixel and the resolution of recorded image is dependent on the number of fibers.

Generally the S/N ratio of borescopic records is considerably smaller than that of camera records. A comparison of camera and endoscope images of black dots on a white background is shown in Fig. 8. Figures 8(d) to 8(f) correspond with Figs. 8(a) to 8(c), respectively, with enhanced image qualities by image processing. Light intensity diagram along the horizontal line passing through the center point is given beneath each image. Compared to the camera image, a borescope image shows a considerable reduction in light intensity distribution and decreased

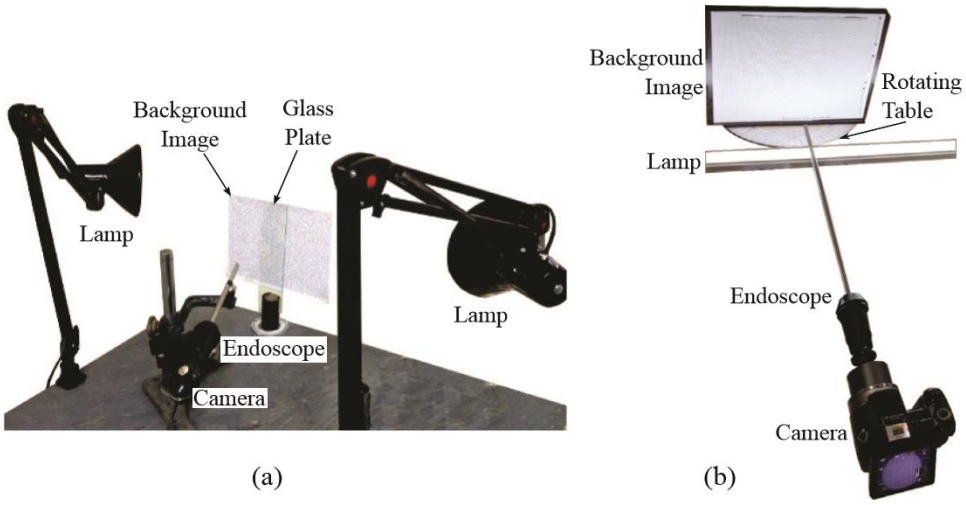

Fig. 9. Experiment setups. Dot pattern displacement measurement with 45°, (a), and 0°, (b), rigid endoscopes. In the left setup (a), the shift of dot patterns is realized by a rotated plate glass between endoscope and background image and in set up (b) the background image is rotated by a rotating table, while the plate glass (not shown) remains perpendicular to the endoscope axis. Configuration (b) can be modified to fix the background image and rotate the plate glass by the rotating table.

S/N ratio. The quality of images and the type and distribution of image noise is better visible in the processed images 8(d) to 8(f). Compared to camera and rigid borescope images, the images of flexible borescope, Fig. 8(c) and 8(f), show reduced resolution and S/N ratio.

3.3 Endoscopic BOS Measurements

In this section the technical aspects of endoscopic BOS is presented. Figure 9 shows two experiment setups. A 45° rigid endoscope, Fig. 9(a), captures the dot pattern displacements caused by the rotation of a plate glass between the background image and endoscope head. Figure 9(b) shows a 0° rigid endoscope and a rotated image plane. In this setup, the plate glass (not shown) between endoscope head and background plane can remain fixed, while the background plane rotates by a rotating table, in order to investigate image distortion at different angles. Alternatively the background plane can remain fixed and the plate glass can be rotated by the rotating table to measure dot shifts.

Figure 10(a) shows a rectangular calibration grid. The recorded image of this grid by borescope is shown in Fig. 10(b). The curved lines in this image indicate that the distortion of image is not linear. Image distortion varies with the borescope construction and measurement configuration. At inclined viewing angles, such as 45°, the non-linearity of image distortion increases, such that the accuracy of common distortion compensation methods such as quadratic surface fit might be inadequate and higher order methods might be required for accurate image reconstruction. Figure 11 shows a distorted calibration grid and its reconstruction using distortion compensation by partial differential equations, Mohseni (2011). In Fig. 11(b) straight horizontal and vertical lines show the expected exact position of each reconstructed point. These lines are drawn by color inversion so that the actual pixel vales remain visible.

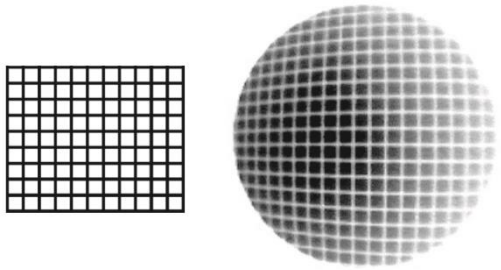

Fig. 10. (a) A grid of perpendicular straight lines, and (b) its image taken by borescope. Significant distortion is seen in the recorded image by borescope in comparison with to the original image. Image (b) is shown inverted.

3.4 Compensation for Noise Effects

As shown in Fig. 8, the noise of endoscopic records is higher than camera records due to reduced light passing through the small aperture of endoscope and longer optical path. Normalization will intensify image noise as shown in Figs. 8(e) and 8(f). Two methods of compensation of the noise effect are adjustment of illumination of image plane and averaging. By increasing the illumination intensity in image plane, the S/N ratio of recorded images increases. Since dot patterns form the measurement signals, higher contrast of artifacts in calibration and background images serves to higher S/N ratio.

Random noise can be compensated by ensemble

averaging. When the subject of imaging is stationary, averaging of several images of the same subject causes the reduction of noise effects. Figure 12(a) shows an endoscopic record of a calibration grid, with non-uniform background illumination. In order to reveal the effect of noise in the image, the color levels have been reduced from 256 to 16. Also color inversion has been applied to every other color strip to facilitate visual perception of noise effect along the borders of each color strip. The effect of noise is seen as random distribution of individual pixels near the strip borders and color fluctuations at the boundaries of each color strip. It is seen that ensemble averaging between a limited number of images, in this case five images, reduces the noise effect considerably, Fig. 12(b).

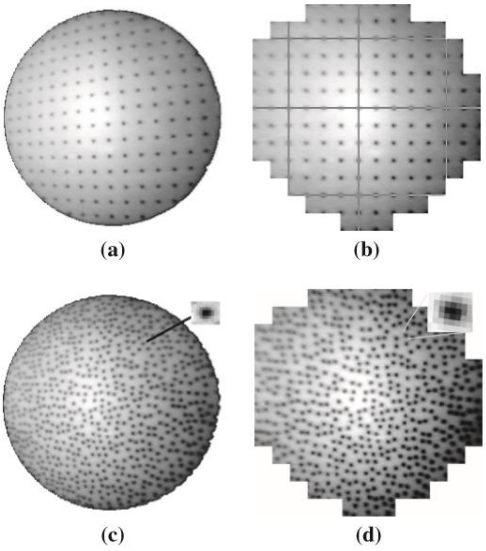

Fig. 11. (a) Borescope image of calibration grid, (b) reconstructed calibration grid. Straight horizontal and vertical lines show the expected exact location of the grid points. (c) Random dot patters recorded by borescope with the same imaging configuration as (a). (d) Reconstructed image (c) showing the deformation of reconstructed pixels.

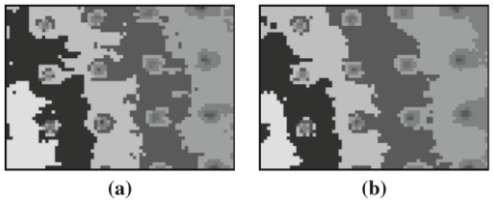

Fig. 12. The effect of noise in borescope record of a calibration plane, consisting of a dot matrix of equal distances in each direction. (a) Original image, (b) averaged image between five images.

Figure 13 shows a comparison between the displacement magnitude contours resulting from the correlation of a single measurement image with a single reference image (dashed lines) and the comparison of a single displacement image with an ensemble-averaged reference image (continuous lines), in which contour borders are more smooth due to reduced noise in the reference image.

Figure 14 shows the shift vectors generated by the rotation of a plate glass in Fig. 9(b). This figure compares the results of particle shift analysis on original images (a) to (c), and on their corresponding reconstructed images (d) to (f). Contours of displacement vector magnitude, δ, together with displacement vectors are shown in Figs. 14(a) and 14(d). Similarly, the displacement vectors and the x and y-components of displacement vector, δ_x and δ_y, are shown in parts (b) and (e), and (c) and (f), respectively.

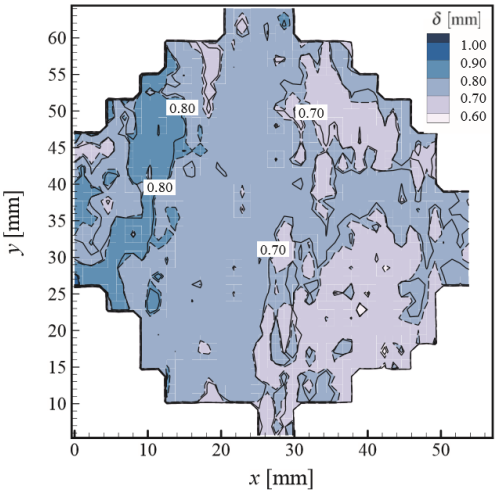

Fig. 13. Comparison between displacement magnitude contours of the correlation of a single measurement image with a single reference image (dashed lines) and the correlation of a single measurement image with an ensemble-averaged reference image (continuous lines).

The rotation of plate glass causes a nearly horizontal shift in dot patterns. Figures 14(a) to 14(c) show the results of correlation analysis on original (distorted) endoscopic records. Contours of displacement magnitude are very similar to the contours of displacement component in x-direction, δ_x, in Fig. 14(b), and both show fluctuations in the contour variables. These fluctuations are caused by the internal noise of image sensor, reduced S/N ratio in endoscopic image, and image distortion. In this experiment, the variation of displacement vectors due to image distortion is higher in the right region of the images 14(a) and 14(b). After reconstruction, these regions appear on the left side of the images, Figs. 14(d) and 14(e), and in the top region of Fig. 14(f), since the direction and magnitude of the displacement vectors have been modified during reconstruction.

To evaluate the effect of noise, Fig. 15 shows a comparison of two displacement vector fields of reconstructed images. Figure 15(a) shows the result of the correlation of two individual images, in which image noise exists, and Fig. 15(b) shows the same

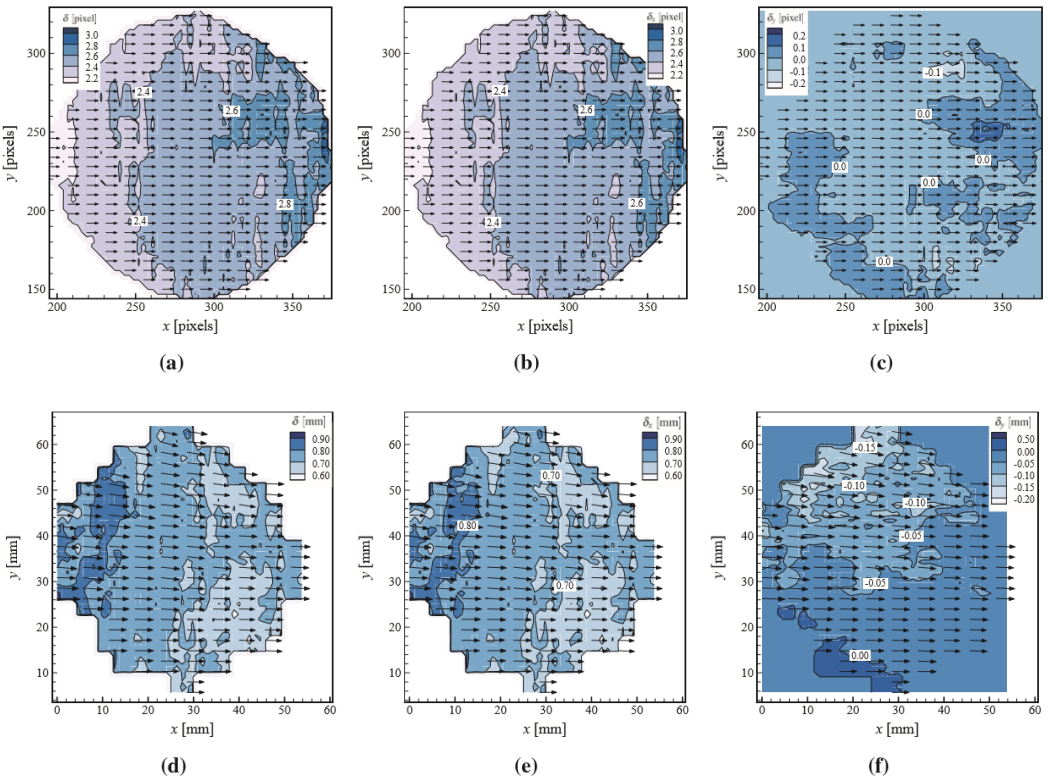

Fig. 14. Analysis of endoscopic particle shift images. In each image the displacement vectors has been shown together with the contours of displacement magnitude, (a) and (d), *x*-component of displacement vector, (b) and €, and *y*-component of displacement vector, (c) and (f). Figures (a) to (c) are original images and correspond to figures (e) to (f), respectively, in which image distortion has been compensated.

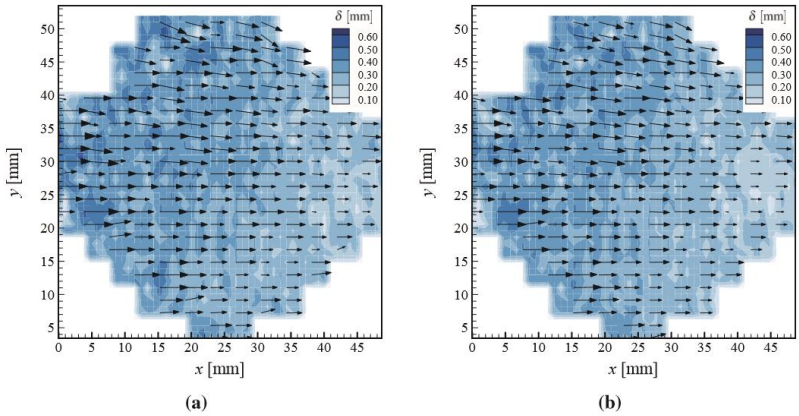

Fig. 15. Comparison of reconstructed vector shifts resulted from correlation analysis of (a) single images, and (b) ensemble averaged images.

vector field, resulted from the correlation of two ensemble averaged images. As a result of averaging, the vectors of Fig. 15(b) are more oriented and more uniform in length, with considerably less fluctuations in vector directions, than in Fig. 15(a). This comparison shows that the effect of image noise in endoscopic records can become considerable. Ensemble averaging of images, when feasible, reduces the noise effect and increases the accuracy of correlation analysis.

A comparison of the application of endoscopic BOS with BOS measurements with camera is illustrated in Fig. 16. Evaporated steam from a hot water bed by natural convection is visualized by regular BOS method using camera, Figs. 16(a) and 16(b), and by endoscopic BOS, Figs. 16(c) and 16(d). Since the steam column is unstable and changes with time, the results present a qualitative comparison between camera and endoscope measurements. Both displacement magnitude, δ , and *x*-component of displacement vector δ_x are shown. The endoscope results, parts (c) and (d), are original records in which image distortion exists.

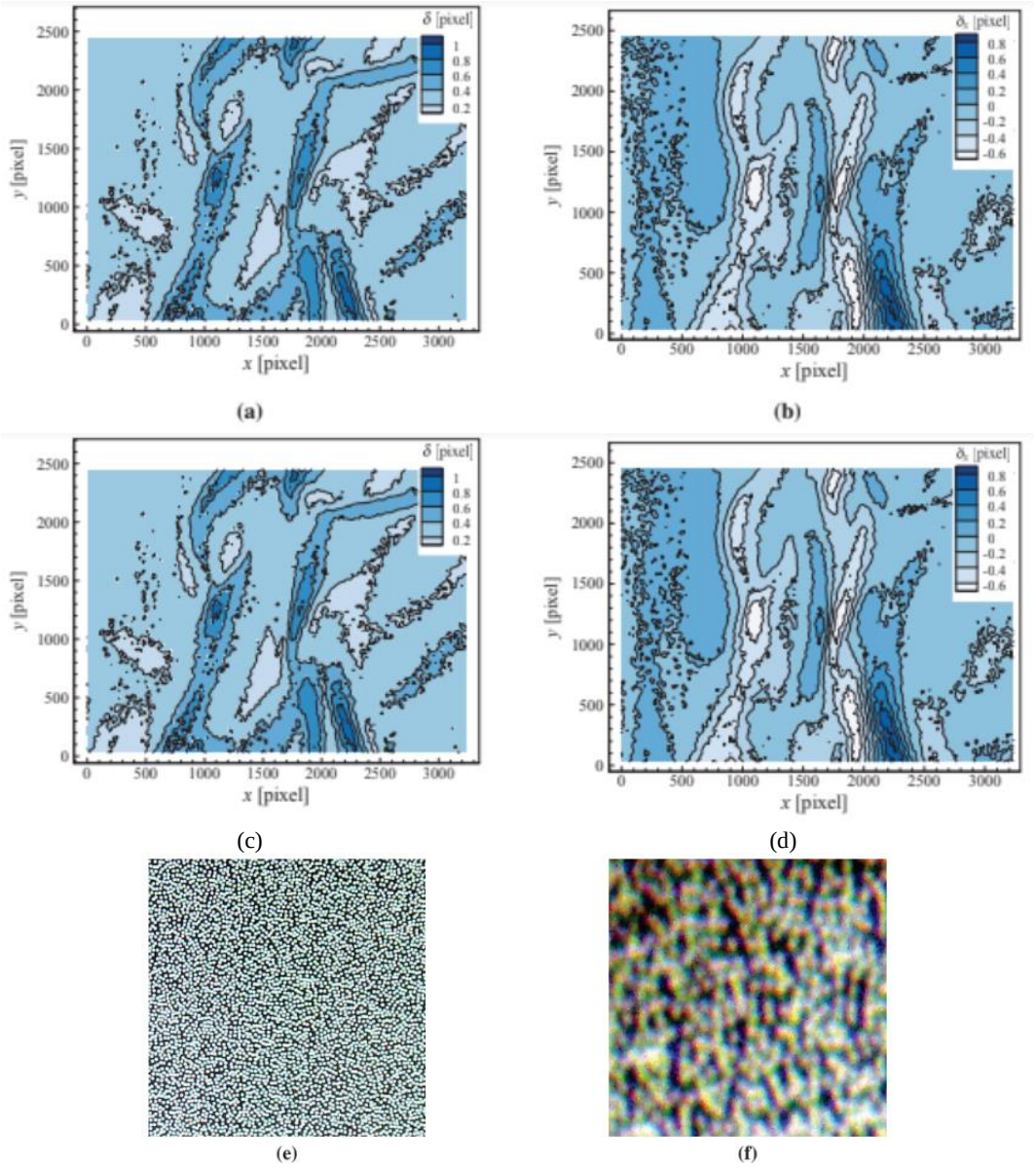

Fig. 16. Comparison of BOS analysis of a steam column evaporating from a hot water bed by natural convection recorded by camera, (a) and (b), and rigid borescope (c) and (d). Parts (a) and (c) show the contours of displacement magnitude, δ , and parts (b) and (d) show the contours of the x-component of displacement vector, δ_x. Samples of camera image, (e), and endoscope image, (f), are shown to compare the quality of particle shift images in camera and endoscope records.

Both measurements show displacements in the order of one pixel and are 3000 pixel × 2500 pixel in size. The quality of borescope image, Fig. 16(f), is considerably lower than the quality of camera image, Fig. 16(e). Also the particle density of borescope image is lower than the camera image. As a result, the quality of captured density field by camera in Fig. 16(a) is considerably degraded in endoscopic measurement depicted in Fig. 16(c).

4. CONCLUSION

In this paper, the applicability of BOS technique to near-field density measurement is investigated via two series of experiments. In the first series, particle shift image pairs are generated by rotating a plate glass in front of camera and endoscope, which provides stable dot pattern shifts of arbitrary sizes. In this series, the quality of images, the effect of image noise, ensemble averaging, and the reconstruction of distorted images were investigated.

In the second series of experiments, an actual density field. i.e. evaporating steam from a bed of hot water was measured by both camera and endoscope. As the result of experiments, endoscopic BOS is highly dependent on the noise of image sensor, image distortion caused by optical setup, captured light intensity by image sensor or the illumination quality

of object. For comparable image sizes of camera and endoscope, the quality of endoscope image is considerably lower than the quality of camera records. Therefore, depending on the quality of measurement setup and setup components, endoscopic BOS measurements can be marginal and an alteration of measurement setting may lead to unsuccessful measurements.

The application of endoscopic BOS for the measurement of flow density variations, such as aerodynamic density fields, is very demanding in terms of optical components, measurement setup, and adjustments and settings.

ACKNOWLEDGMENTS

The authors would like to thank Dr. Mohammad-Hossein Soorgee and Mr. Majid Firouzan from the Faculty of Mechanical and Energy Engineering of Shahid Beheshti University for providing measurement instruments and technical support.

REFERENCES

Bauknecht, A., C. B. Merz, M. Raffel, A. Landolt and A. H. Meier (2014). Blade-tip vortex detection in maneuvering flight using the background-oriented schlieren technique. *Journal of Aircraft* 51(6), 2005-2014.

Berger, K., B. Atcheson, I. Ihrke, W. Heidrich and M. Magnor (2009). Tomographic 4D reconstruction of gas flows in the presence of occluders. In *Proc. Vision, Modeling, and Visualization (VMV'09)*, Braunschweig, Germany.

Goldhahn, E. and J. Seume (2007). The background oriented schlieren technique: sensitivity, accuracy, resolution and application to a three-dimensional density field. *Experiments in Fluids* 43, 241-249.

Goldhahn, E., O. Alhaj, F. Herbst and J. Seume (2009). Quantitative measurements of three-dimensional density fields using the background oriented schlieren technique. In W. Nitsche and C. Dobriloff (Eds.), *Imaging Measurement Methods for Flow Analysis*, pp. 135–144. Springer-Verlag.

Hargather, M. J. and G. S. Settles (2010). Natural-background-oriented schlieren imaging. *Experiments in Fluids* 48, 59-68.

Heidari, M. R., M. R. Soltani, M. Farahani and M. Taeibi-Rahni (2010). Computational and experimental investigations of boundary layer tripping. *Journal of Applied Fluid Mechanics* 3(2), 53-63.

Kindler, K., E. Goldhahn, F. Leopold and M. Raffel (2007). Recent developments in background oriented schlieren methods for rotor blade tip vortex measurements. *Experiments in Fluids* 43, 233-240.

Meier, G. E. A. (1999), *Hintergrund-Schlierenmeßverfahren (Background-Oriented Schlieren Technique)*, German Patent, No. DE 199 42 856 A1, Germany.

Meier, G. E. A. (2002). Computerized background-oriented schlieren. *Experiments in Fluids* 33, 181–187.

Merzkirch, W. (1987). *Flow Visualization* (2nd Ed. ed.). Academic Press Inc.

Mohseni, A. (2011). *Development of Endoscopic Stereoscopic PIV for Investigating the IGV-Impeller Interaction in a Centrifugal Compressor*, Südwestdeutscher Verlag für Hochschulschriften, Germany.

Ota, M., K. Hamada, H. Kato and K. Maeno (2011). Computed-tomographic density measurement of supersonic flow field by colored-grid background oriented schlieren (CGBOS) technique. *Measurement Science and Technology* 22(10), 104011 (7 pages).

Ota, M., K. Kurihara, K. Aki, Y. Miwa, T. Inage and K. Maeno (2015). Quantitative density measurement of the lateral jet/cross-flow interaction field by colored-grid background oriented schlieren (CGBOS) technique. *Journal of Visualization* 18, 543-552.

Raffel, M. (2015). Background-oriented schlieren (BOS) techniques. *Experiments in Fluids* 56(60), 1–17.

Raffel, M., J. Kompenhans, S. T. Wereley and C. E. Willert (2007*). Particle Image Velocimetry: A Practical Guide* (2nd Ed. ed.). *Exp. Fluid Mech*. Springer.

Richard, H. and M. Raffel (2001). Principle and applications of the background oriented schlieren (BOS) method. *Measurement Science and Technology* 12, 1576-1585.

Richard, H., M. Raffel, M. Rein, J. Kompenhans, and G. E. A. Meier (2002). Demonstration of the applicability of a background oriented schlieren (BOS) method. In R. J. Adrian, D. F. G. Durao, M. V. Heitor, M. Maeda, C. Tropea, and J. H. Whitelaw (Eds.), *Laser Techniques for Fluid Mechanics*—Selected Papers from the 10th International Symposium Lisbon, Portugal, July 10-13, 2000, pp. 145-156. Springer-Verlag Berlin Heidelberg.

Saiprakash, M., C. SenthilKumar, G. K. Sunil, S. P. Rampratap, V. Shanmugam and G. Balu (2019). Visualization of shock wave phenomenon around a sharp cone model at hypersonic Mach number in a shock tunnel using high speed schlieren facility. *Journal of Applied Fluid Mechanics* 12(2), 461-468.

Saleh, B. E. A. and M. C. Teich (2007). *Fundamentals of Photonics* (2nd Ed. ed.). John Wiley & Sons.

Settles, G. S. (2001). *Schlieren and Shadowgraph Techniques*. Springer-Verlag, Germany.

Skornyakova, N. M., E. M. Popova, B. S. Rinkevichyus and A. V. Tolkachev (2004). The investigation of heat transfer by background oriented schlieren method. In *Proceedings of the 12th International Symposium on Application of Laser Techniques to Fluid Mechanics*, Lisbon. CD-ROM.

Sommersel, O. K., D. Bjerketvedt, S. O. Christensen, O. Krest and K. Vaagsaether (2008). Application of background oriented schlieren for quantitative measurements of shock waves from explosions. *Shock Waves* 18, 291–297.

Su, C. and J. Bai (2016). Measurement of the neutral plane of an internal fire whirl using the background-oriented schlieren technique for a vertical shaft model of a high-rise building. *Measur.* 78, 151–167.

Tipnis, T. J., M. V. Finnis, K. Knowles and D. Bray (2013). Density measurements for rectangular free jets using background-oriented schlieren. *The Aeronautical Journal* 117(1194), 771–784.

Tropea, C., J. F. Foss and A. L. Yarin (2007). Springer *Handbook of Experimental Fluid Mechanics*. Springer.

Venkatakrishnan, L. and G. E. A. Meier (2004). Density measurements using the background oriented schlieren technique. Experiments in Fluids 37, 237-247.

Vinnichenko, N. A., A. V. Uvarov and Y. Y. Plaksina (2014). Combined study of heat exchange near the liquid-gas interface by means of background oriented schlieren and infrared thermal imaging. *Experimental Thermal and Fluid Science* 59, 238–245.